

GPU Assisted Fast and Robust 3D Image Registration of Large Wet and Dry Rock Images Under Extreme Rotations

Muhammad Sarmad^{a,*}, Johan Phan^{a,b}, Leonardo Ruspini^b, Gabriel Kiss^a and Frank Lindseth^a

^aNTNU, Høgskoleringen 1, Trondheim, 7491, Norway

^bPetricore, Stiklestadveien 1, Trondheim, 7041, Norway

ARTICLE INFO

Keywords:

Dry-wet image registration

Digital rock analysis

Pytorch

AirLAB

ABSTRACT

Image registration is a process used to align or register multiple images or volumes to facilitate comparison or combination of the data. In the context of 3D wet and dry images of rock samples, it is essential to accurately align these images to analyze and utilize the data in various experiments. These images can be huge and contain minimal corresponding key points in the wet and dry images. A lack of these key points makes the registration problem extremely difficult. Traditional intensity-based optimization-based methods for image registration can be slow, while deep learning-based "one shot" methods fail due to a lack of key points and training data.

We propose a new optimization-based algorithm for image registration of large 3D wet and dry images of rock samples to address these issues. Our algorithm can handle extreme rotations of the samples and even complete inversion along horizontal axes. Additionally, it is optimized for speed while maintaining high accuracy by utilizing a graphical processing unit (GPU). We have demonstrated that our algorithm can provide a solution in under a minute for samples of size 1000^3 cube, compared to the several hours of expert time needed by the current industrial practice. We provide quantitative and qualitative results and compare our algorithm to the solution time of a human expert.

1. Introduction

Digital rock analysis is a sub-field in the geology field that involves using advanced imaging techniques to analyze rocks and other geological materials at a microscopic level. These techniques allow geologists to study rocks' internal structure and composition in great detail, which can provide valuable insights into the physical and chemical processes that have shaped the Earth's crust over time. Digital rock analysis can be used to study various rocks, including sedimentary, metamorphic, and igneous rocks. It can be applied to various research areas, including hydrocarbon reservoirs, environmental geology, and geomechanics. Some of the main techniques used in digital rock analysis include X-ray computed tomography (CT), scanning electron microscopy (SEM), and micro-computerized tomography (micro-CT).

Digital rock analysis often begins with creating an accurate 3D porosity model based on porous media X-ray images. This model can calculate various physical and fluid flow properties through image analysis techniques and flow simulations. This approach can be faster and less destructive than traditional laboratory measurements. However, when working with complex porous materials such as reservoir rocks, it is often necessary to use multiple X-ray images due to the wide range of pore sizes present in the sample. Additionally, it is typical for micro-CT images of rocks to have a significant portion of the percolating porosity below the resolution limit, making it challenging to model the pore network accurately Aarnes et al. (2007). Using a dry-wet

image pair is common to obtain a more accurate porosity image in such cases. It can explain how the pore network changes as the rock absorb fluids. Feali et al. (2012); Long et al. (2013); Bhattad et al. (2014); Ruspini et al. (2021).

In dry-wet imaging, a sample is first scanned using X-rays while it is dry and then re-scanned after it has been saturated with a high X-ray attenuation fluid, such as brine. Comparing the images taken at these two states makes it possible to create a map showing the porosity level at each voxel. However, one of the main challenges of this imaging technique is the need for image registration, which is the process of aligning the images taken in the dry and wet states. This procedure is necessary because the wet sample must be aligned with the dry sample to compare the two states accurately.

Dry-wet imaging is a powerful technique in digital rock analysis, but it also presents several challenges in terms of image registration. The significant differences between the dry and wet images, as well as the relatively homogeneous nature of rock images at the texture level, can make it difficult to use feature point matching techniques for alignment. Additionally, the large size of 3D images obtained from micro CT, which can contain billions of voxels and multiple gigabytes of data, makes it resource-intensive to load and manipulate these images. This can hinder the performance of automated registration algorithms and require a significant amount of expert labor. Improving the image registration process for digital rock analysis is therefore important for streamlining the digital rock workflow and reducing the amount of labor required.

In this work, we aim to address the unique challenges associated with image registration in dry-wet imaging for digital rock analysis. Specifically, we recognize that the

*Corresponding author

✉ muhammad.sarmad@ntnu.no (M. Sarmad); johan.phan@ntnu.no (J. Phan); leonardo.ruspini@petricore.com (L. Ruspini)
ORCID(s): 0000-0002-8635-9000 (M. Sarmad)

significant textural differences between the dry-wet images, extreme misalignments, and large image sizes can make it difficult to align these images quickly using traditional techniques. To address these challenges, we propose a solution based on a GPU-accelerated implementation of an intensity-based registration algorithm. This approach allows for fast, robust and accurate image registration in a practical setting. Our contributions are summarized as follows:

- Our method accurately performs image registration for dry-wet image pairs of various textures.
- Our algorithm can find a solution in under one minute by utilizing a graphical processing unit (GPU) for optimization.
- The algorithm can handle extreme rotation along the vertical axis of cylindrical samples, as well as inversion along the horizontal axes of the sample.
- Evaluations on various datasets demonstrate our algorithm's performance. We also compare the method to a human expert who takes more than one hour for the same task.

2. Related Work

Common techniques for unimodal images include correlation methods, as described in Pratt (1974). These methods often require additional cleaning steps to ensure the success of cross-correlation. Althof et al. (1997) demonstrated that automatic and fast solutions with reasonable accuracy can be achieved through correlation-based methods. For multimodal images, Viola and Wells III (1997) and Maes et al. (1997) proposed the use of mutual information, which is more robust to such images. Fourier-based methods, which work with the Fourier representation of images, are faster than cross-correlation methods De Castro and Morandi (1987). Jenkinson and Smith (2001) focused on the optimization algorithm itself and tailored a global optimization algorithm specifically for registration. The choice of similarity measure (e.g., correlation vs mutual information) is crucial for the success of registration, and Roche et al. (2000) provided guidance on how to select the correct measure for the best results. While these methods are effective, they can require a number of iterations to reach the final result. In this work, we also utilize optimization-based methods, but leverage the power of graphical processing units (GPUs) through the use of open-source libraries Pytorch Paszke et al. (2017) and AIRLab Sandkühler et al. (2018) for gradient calculation required for optimization.

Deep learning has been a popular choice for solving many registration problems since convolutional neural networks (CNN) have become popular Krizhevsky et al. (2012); LeCun et al. (1990). Learning-based methods have been used for every stage of the registration process. Haskins et al. (2019) propose to learn the similarity metric using a CNN while keeping the classical optimization process. On the other hand, Miao et al. (2016) and Chee and Wu (2018)

use a synthetic transform-based data generation method to train a CNN model that predicts the transformation matrix in one shot. Liao et al. (2017) utilize a reinforcement learning-based method to train an agent for robust image registration. These methods mostly use medical image datasets and are impressive as they are fast at inference time. However, they do not work well with our dataset due to the lack of enough distinguishing features in the dry and wet images. There are unsupervised approaches for deformable image registration as well Hu et al. (2018). However, we are limited to rigid transform. Haskins et al. (2020) and Fu et al. (2020) present a through survey on learning based approaches.

Image registration is the first step in many problems where the properties of the rock need to be estimated Knackstedt et al. (2004); Arns et al. (2002); Padhy et al. (2007); Prodanović et al. (2007). Even though the problem of image registration has been solved in the medical image domain by many methods, that is not the case for wet and dry image registration. The seminal work of Latham et al. (2008) uses a correlation-based method coupled with an optimizer to perform 3D dry image to wet image registration which is slow due to the iterative nature of the optimization process. We bring the time from hours to seconds due to using a graphical processing unit (GPU).

Our work is based on the open-source library AIRLab Sandkühler et al. (2018). However, other toolboxes are also available, e.g. ITK Yoo et al. (2002), Elastix Klein et al. (2009), and ANTs Avants et al. (2011). However, these toolboxes and libraries do not utilise the GPU transparently and efficiently as AIRlab. Therefore, prototyping in these methods is time-consuming and error-prone, which can be problematic in an industrial setting. For a detailed review of other toolboxes available for the task of registration, we refer to Keszei et al. (2017).

3. Method

In this section, we provide the detailed working of our registration algorithm. The problem overview is shown in Fig. 1. We solve the problem of Dry-Wet Image registration. Consider a dry image Im_{Dry} . This image is a micro CT scan of a rock sample. This sample can then be imbibed with liquid, e.g. brine or mercury, to obtain a wet image Im_{Wet} of the same rock sample. The injection of liquid in this sample changes the visual characteristics of this sample to a large extent under a micro CT. This phenomenon can be seen in the figure.

Fig. 1 shows a perfectly registered dry and wet image pair as the output of the registration process on the right side of the image. A close examination of the registered images reveals that the regions in the Dry-Wet image pair that correspond well are sparse. Secondly, the regions that correspond to each other in both samples reside in different colour spaces. This input setting can lead to a problem for intensity-based methods since they rely on these visual cues to determine a feasible solution through optimization. Therefore, we utilize pre-processing steps before registration

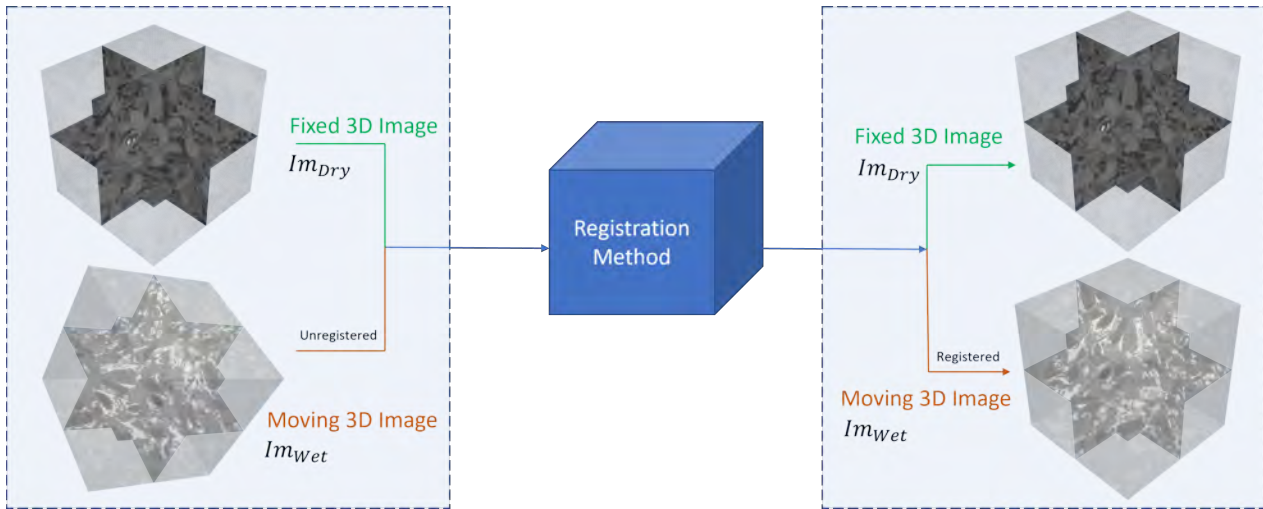


Figure 1: We solve the problem of Dry-Wet rock Image registration. Our Registration Method (Blue box) can register Image pairs efficiently and accurately. In this figure, the Fixed 3D Image is the Dry Image, whereas the Moving 3D Image is the Wet Image. The registration method finds the transformation required to warp the Moving 3D image to register it to the Fixed 3D Image.

to ensure that the optimization-based registration algorithm works robustly. The pre-processing steps are given as follows:

Color Inversion and Histogram Matching We observe from Fig. 1 that the wet image and dry image correspond with each other. However, the colours seem inverted. Therefore, we invert the colours of the wet image to ensure that it corresponds well with the dry image. We note that a simple inversion of the images is not sufficient. The histogram of the wet-dry image pair must be matched prior to the execution of the registration algorithm. The raw images from the CT scan are provided in a 16-bit unsigned raw format. This format means that the possible values can range from 0 to 65535. Metallic regions with a high atomic number have high pixel values associated with them in the 3D image, whereas the material with a low atomic number has a lower value. In the case of the rock sample of concern, metal objects often shine very bright and distort the colour of the remaining vital regions, such as pores and solids in the rock samples. Therefore to get the best possible match between the dry-wet images, we match the histogram of the wet image to the dry image.

Table 1 shows a thorough comparison between dry and wet images before and after the operation of colour inversion and histogram matching. This comparison has been performed on all datasets used in this work. The details of each dataset will be provided in the experiment section. It can be seen that the colour shift between dry-wet pairs is a colour inversion in all cases. The matching regions are made more prominent after an inversion of colours. We always perform this procedure for the Wet image only. After the inversion, the results of this operation are shown in the column ‘Inverted W’ in Table 1. It can be seen that in the row ‘ST C14’, the ‘Wet Image (W)’ seems washed out after inversion. This is because of the metallic regions (white

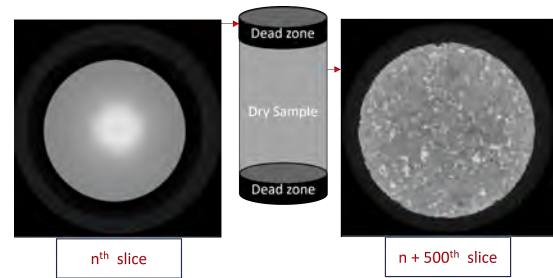


Figure 2: Deadzone: A microCT image of a sample contains dead-zones of variable length due to padding material placed at the end to hold sample in place.

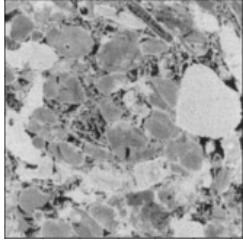
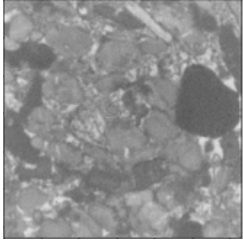
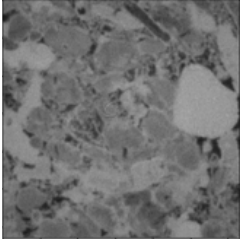
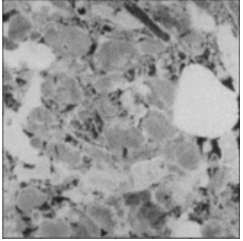
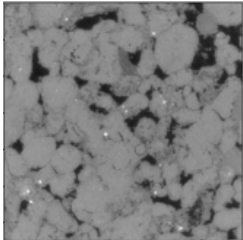
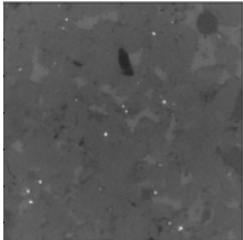
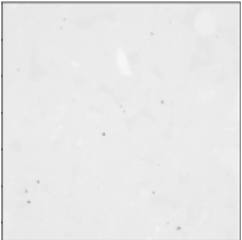
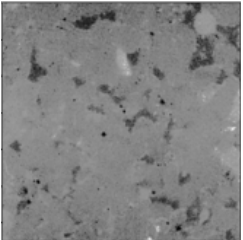
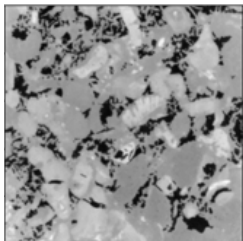
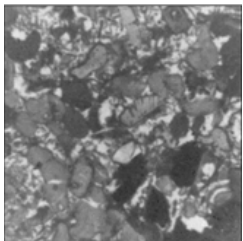
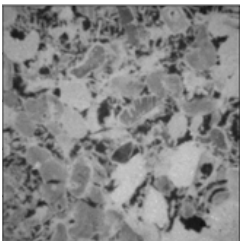
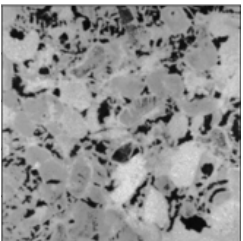
spots) in the ‘Dry Image (D)’. Therefore, we apply histogram matching to solve this problem. After applying histogram matching, we observed that the ‘Histogram Matched (W)’ image corresponds well with the ‘Dry Image (D)’.

Dead Zones A special consideration for image registration in digital rock analysis is the existence of so-called ‘dead zones’ as shown in Fig. 2. These exist since the cylindrical sample is padded on top and bottom before putting the sample inside a CT scan. This extra padding leads to blank regions included in the final image. These regions must be considered to ensure that they do not negatively affect the automatic registration process.

Extreme Transformation Another aspect that makes our problem different from typical 3D image registration is the characteristic of the transformation. The transformation is a similarity transformation in nature. This setting means that there are nine elements in the transformation. These include translation, rotation and scaling for their respective axes. Of particular importance are the rotations as shown in Fig. 3. Along z-axis, this rotation can be $\pm 180^\circ$. Since the wet sample can be placed at any angle. The second important

Table 1

Image Samples from each of the dataset used have been shown in this table. The Dry Image (D) and Wet Image (W) do not correspond with each other. The Colors of Wet Image are inverted and shown in Column 'Inverted W'. The Inverted W image's histogram is matched to Dry Image (D) to create 'Histogram Matched W' Image.

Dataset \ Image	Dry Image (D)	Wet Image (W)	Inverted W	Histogram Matched W
Wang et al. (2021)				
ST C14				
Spurin et al. (2021)				

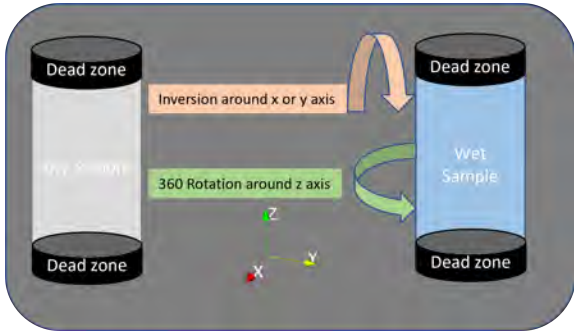


Figure 3: Extreme Rotation: A microCT image of a wet and dry sample are shown. Note that The wet sample can have extreme rotation of $\pm 180^\circ$ along z-axis and a 180° inversion around the x or y axes.

aspect is the possible inversion of the sample along the x or y axes. This means that a 180° inversion of the sample is also possible.

3.1. Registration Algorithm

After the pre-processing steps mentioned before, the samples are ready for registration. We use the normalized cross correlation between the dry and wet image to find the perfect matching. The details are given in algorithm

1. We utilize the similarity transformation along with the normalized cross-correlation similarity objective which is given as follows:

$$\mathcal{L}_{NCC} := \frac{\sum Im_{Dry} \cdot (Im_{Wet} \circ f) - \sum E(Im_{Dry})E(Im_{Wet} \circ f)}{|\mathcal{Y}| \cdot \sum Var(Im_{Dry})Var(Im_{Wet} \circ f)} \quad (1)$$

The sum in the above mentioned equation is over over the image domain \mathcal{Y} , E is the expectation value (or mean) and Var is the variance of the respective image. The registration algorithm aims to find the best match between the two 3D images. For the scope of this work, the dry and we image can contain translation of about 40 pixels in the x and y axes. Only 5 pixels in the z axis. A uniform scaling factor of 0.95 to 1.05 can also be present along any of the three axes. Rotation along x-axis and y axis can be about $\pm 5^\circ$. If the samples are inverted about x-axis or y-axis, the rotation can still be about $\pm 5^\circ$. The rotation along z axis can be a $\pm 180^\circ$. We design our method to be suitable for the worst case scenario. It assumes two worst case scenarios i.e. it contains a rotation of $\pm 180^\circ$ about the z axis and the second is that the sample to be registered is inverted about the x or y axis as shown in Fig. 3.

Algorithm 1: How to write algorithms

```

 $L_{best} = \infty$  ;
 $\delta_\theta = 20 \text{ deg}$  ;
 $S_{best} = 0$  ;
 $Iter_{init} = 25$  ;
 $Iter_{final} = 100$  ;
 $Lr_{init} = 0.01$  ;
 $Lr_{final} = 0.0005$  ;
 $Im_{Dry}$  and  $\tilde{Im}_{Wet}$  ;
 $L, S_j = \text{LocalRegistration}(F_{Invert} = \text{False})$ ;
 $\tilde{L}, \tilde{S}_j = \text{LocalRegistration}(F_{Invert} = \text{True})$ 
if  $L \leq \tilde{L}$  then
    |  $L_{best} = L$ ;
    |  $S_{best} = S_j$  ;
else
    |  $L_{best} = \tilde{L}$ ;
    |  $S_{best} = \tilde{S}_j$  ;
end
Rotate  $\tilde{Im}_{wet}$  by  $\delta_\theta \times S_{best}$  along z-axis ;
 $Loss_{NCC}$ ;
Optimizer( $Lr_{final}$ );
Similarity Transformation Registration( $Iter_{final}$ );
Function  $L_{best}, S_{best} =$ 
LocalRegistration( $F_{Invert}$ ):
    |  $L_{current} = 0$ 
    |  $S_j = 0$ 
    | for  $S_j \leq \frac{360}{\delta_\theta}$  do
        | Rotate  $Im_{wet}$  by  $\delta_\theta \times S_j$  along z-axis ;
        |  $Loss_{NCC}$ ;
        | Optimizer( $Lr_{init}$ );
        | Rigid Transformation Registration( $Iter_{init}$ );
        | Update  $L_{current}$  ;
        | if  $L_{current}$  is less than  $L_{best}$  then
            | |  $L_{best} \leftarrow L_{current}$  ;
            | |  $S_{best} \leftarrow S_j$ ;
        | else
            | | pass;
        | end
        |  $S_j = S_j + 1$ 
    | end
end

```

Sector Search For Rotation about Vertical Axis We first describe how to deal with the first scenario i.e. rotation about the z axis. . This scenario can occur if the operator places the sample after rotating it in the CT chamber for obtaining the Wet image. The rotation about the z-axis can be determined by the NCC loss based optimization. However, we notice that if the rotation in the z-axis is more than $\pm 10^\circ$ then the algorithm starts to fail. Therefore we propose a localized registration check, where we divide the image to be registered into sectors. The chunk of each sector corresponds to a angle δ_θ . We set this angle empirically to a value that does not break the algorithm. We then check all sectors until a 360° rotation is complete about the z axis. We also log the

scores of matching of each sector using the NCC loss. At the end of this process, we get a best sector. We use the best sector ID to rotate the image to be registered to the best sector for a more fine registration for $Iter_{final}$ iteration. Note that since this is an initial step therefore we do not perform a lot of iteration and only use $Iter_{init}$. Where as in the final iteration step we use $Iter_{final}$ such that $Iter_{init}$ are significantly less than $Iter_{final}$. We call this step a 'sector search'.

Sector Search Inversion about Horizontal Axis The second extreme scenario is that the image to be registered is inverted along the horizontal axis (i.e. x or y axis). This scenario can occur if the operator places the sample upside down in the CT chamber for obtaining the Wet image. To handle this we first perform sector search without inverting the image to be registered and log the best loss value achieved. Later we perform a sector search after inverting the image to be registered and again log the best loss. Finally we compare the loss value achieved by both the inverted and original sector search to determine the correct sector and if inversion is needed or not.

Once the registered image is catered for extreme rotations. We perform a final set of iterations $Iter_{final}$ to find all elements of the similarity transformation namely 3 translation, 3 rotations and 3 scaling factors. The detailed steps of our method are given in the algorithm 1. Please note that L_{best} is the best loss value achieved, δ_θ is the angle in degree that , S_{best} is the best sector, $Iter_{init}$ are the initial iterations used for sector search and inversion, Lr is the learning rate used for optimization algorithm.

4. Experiments and Results

4.1. Open Source Libraries

We utilize AIRLab Sandkühler et al. (2018) for the registration algorithm. It allows for fast prototyping and utilization of GPUs since it utilizes Pytorch Paszke et al. (2017). Our program's execution is finished in under a minute due to the utilization of GPU. We also use Pytorch Paszke et al. (2017) and MONAI Consortium (2020) libraries for creating transformations in the dataloader on the moving Image for validation of our approach.

4.2. Dataset

This work considers various types of dry and wet 3D images of rocks. We use two open-source datasets freely available from Wang et al. (2021) and Spurin et al. (2021). In addition, we utilize an in-house dataset of rock samples which we call the ST C14 dataset. The dimensions of images in these datasets are shown in the Table. 2. All samples are imbibed with fluids such as water or brine to obtain the wet image. For each sample, we have two perfectly registered dry and wet 3D image pairs of the same dimension.

Table Table. 1 shows the detailed pre-processing steps for images. As shown in the Table, we only process the Wet Image by first inverting the colour of the Wet Image. However, this is not enough, and we additionally perform Histogram matching by matching the histogram of the Wet

Table 2

DataSet: Dimensions (in Pixels) and Properties Of the Dataset used

Data-set	x	y	z
Wang et al. (2021)	630	630	1087
ST C14	1300	1300	2500
Spurin et al. (2021)	445	445	445

Image with the Dry Image. The corresponding image is shown in the column ‘Histogram Matched W’.

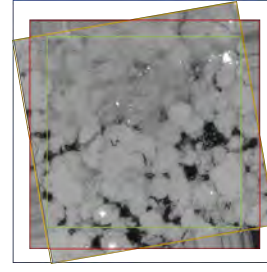
4.3. Dataset Generation for Evaluation

To evaluate the effectiveness of our algorithm, we need to create many possible combinations of three translations, three rotations and one scaling. Please note that the three rotations about x and y can include a possible inversion of the image. At the same time, the rotation about the z-axis can be a 360-degree rotation. We use the three perfectly registered samples in our dataset and transform the wet image randomly on the fly using the a custom Pytorch data loader Paszke et al. (2017). This provides us with a large number of transformations to evaluate our dataset. We limit the randomly generated data transformations to 200 for each of the three datasets.

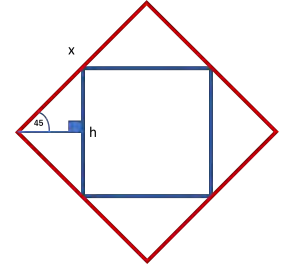
Padding Requirement: Padding the moving image is essential before transforming the image with the data loader since every transformation causes some amount of image information loss near the image border. The padding requirement for synthetic translation and scaling is linearly related to each parameter’s value. However, a unique challenge from a rotation can be observed in Fig. 4a. Consider an original image as shown in red lines. Upon rotation, the image becomes an image shown in yellow lines. However, the image we can utilize after rotation is in green lines due to information loss due to rotation. This image is smaller than the intended size of the image. In order to get an image of the size shown in red lines. We need to start with an image of the size shown in blue lines.

Consider the Fig. 4b, where the image with red lines of size x has been rotated by 45° ; then we can extract the image with blue lines of size h from this square. It can be seen that when we rotate an image by a certain angle, some parts of the image are permanently lost due to the rotation operation. Therefore, we must calculate the padding value p needed to add to the original image of size h such that when starting with an image of size $x = h + p$, we obtain a rotated image which can be cropped by p to obtain a final image of size h such that no loss of information occurs. The calculation of this pad factor p will be maximum when θ is 45° as shown in Fig. 4b. It can be seen that $h = x * \sin(45^\circ)$. Then since $x = h + p$, the pad factor p can be given as follows:

$$p = h \times \left(\frac{1}{\sin(45^\circ)} - 1 \right) \quad (2)$$



(a) Why padding is needed?



(b) Padding factor

Figure 4: Fig.4a demonstrates that loss of image information occurs due to rotation. Fig.4b shows how to derive a padding factor p such that starting from image of size $x = h + p$ we obtain h after cropping with p without loss of any information

To scale this value to be dynamic from 0° to 45° . We use a scale factor based on the angle θ as follows:

$$p = h \times \left(\frac{1}{\sin(45^\circ)} - 1 \right) \times \sin(2\theta) \quad (3)$$

4.4. Metric

We use the root mean square error (RMSE) metric between the ground truth and the predicted transformations to report our algorithm’s performance in registering various dry and wet rock images on the dataset. The formula of RMSE is $\sqrt{\frac{1}{n} \sum_{i=1}^n (y_i - \hat{y}_i)^2}$.

4.5. Quantitative Results

We used the synthetic data described in the previous section to generate various transformations, including extreme transformations such as rotation about the z-axis and complete inversion about the x-axis and y-axis. We compare each transformation prediction’s root mean square error (RMSE) and ground truth transformation. We use 200 random transformations for each rock dataset to find the predicted transformation parameters for the registration task. The results in Table 4 demonstrate the RMSE value for each transformation quantity. It can be noted that ST C14 is a relatively tricky sample. It is not surprising, as it can be seen from Table 1 that ST C14 contains fewer correspondences and therefore is naturally a complex sample to register. From the table, it can be observed that our algorithm performs robustly. This method is robust enough to be deployed in the industry to solve the registration of wet and dry images.

4.6. Qualitative Results

Table 3 shows the qualitative results of our method. It should be noted that both qualitative and quantitative values for each example are given. This gives a good idea of real-term performance. e.g. note that for ST C14, the error seems more significant for specific transformation parameters compared to the rest of the samples from other data set. However, visual inspection reveals that the results are very accurate in reality.

Table 3

The performance of our method on image samples from each dataset is shown in the table. The algorithm calculates the transformation needed to warp the 'Moving Image' and align it with the 'Fixed Image'. The table compares the warped moving image with the 'Ground Truth (GT) Moving Image' and displays the quantitative parameters of the transformation: translation in x, y, and z in pixels (Trans X, Trans Y, Trans Z), rotation in x, y, and z respectively in degrees (Angle X, Angle Y, Angle Z), and scaling in x, y, and z respectively (Scale X, Scale Y, Scale Z).

Dataset	Image	Fixed Image	Moving Image	Warped Moving Image	GT Moving Image	Parameter	Prediction	Ground Truth
Aarnes et al. (2007)						Trans X :	-27.73	-28.00
						Trans Y :	1.04	1.00
						Trans Z :	-16.20	-16.00
						Angle X :	-4.83	-4.82
						Angle Y :	177.09	177.06
						Angle Z :	80.91	80.88
						Scale X :	1.05	1.04
						Scale Y :	1.05	1.04
						Scale Z :	1.04	1.04
Aarnes et al. (2007)						Trans X :	10.22	10.00
						Trans Y :	-27.92	-28.00
						Trans Z :	-16.92	-17.00
						Angle X :	-1.93	-1.93
						Angle Y :	1.15	1.13
						Angle Z :	-57.06	-57.00
						Scale X :	1.03	1.02
						Scale Y :	1.03	1.02
						Scale Z :	1.03	1.02
Aarnes et al. (2007)						Trans X :	27.89	28.00
						Trans Y :	-12.35	-12.0
						Trans Z :	3.15	3.00
						Angle X :	-4.74	-4.74
						Angle Y :	-3.36	-3.36
						Angle Z :	162.23	162.23
						Scale X :	1.02	1.02
						Scale Y :	1.02	1.02
						Scale Z :	1.03	1.02
Aarnes et al. (2007)						Trans X :	-6.10	-5.00
						Trans Y :	3.80	3.00
						Trans Z :	-9.88	-10.00
						Angle X :	-3.34	-4.38
						Angle Y :	0.16	-0.78
						Angle Z :	93.23	94.17
						Scale X :	1.08	0.97
						Scale Y :	1.01	0.97
						Scale Z :	1.00	0.97
Aarnes et al. (2007)						Trans X :	-4.49	-3.00
						Trans Y :	-0.50	-1.00
						Trans Z :	2.06	3.00
						Angle X :	-0.69	-1.59
						Angle Y :	179.69	178.57
						Angle Z :	-90.27	-87.77
						Scale X :	1.03	1.00
						Scale Y :	1.07	1.00
						Scale Z :	1.14	1.00
Aarnes et al. (2007)						Trans X :	-7.92435	-10.0
						Trans Y :	10.66	11.00
						Trans Z :	-2.86	-2.00
						Angle X :	3.33	3.94
						Angle Y :	0.34	0.85
						Angle Z :	-7.11	-7.87
						Scale X :	1.00	0.98
						Scale Y :	1.00	0.98
						Scale Z :	1.03	0.98
Aarnes et al. (2007)						Trans X :	-10.71	-10.00
						Trans Y :	-8.17	-9.00
						Trans Z :	9.45	10.00
						Angle X :	2.70	2.23
						Angle Y :	184.28	184.14
						Angle Z :	-35.39	-35.77
						Scale X :	1.06	0.99
						Scale Y :	1.02	0.99
						Scale Z :	1.02	0.99
					Trans X :	-13.29754	-13.0	
					Trans Y :	-16.31	-16.00	
					Trans Z :	-5.65	-6.00	
					Angle X :	-1.14	-1.76	
					Angle Y :	-1.25	-1.75	
					Angle Z :	128.61	128.53	
					Scale X :	1.02	0.98	
					Scale Y :	0.98	0.98	
					Scale Z :	0.99	0.98	
					Trans X :	0.70478	1.0	
					Trans Y :	1.92	2.00	
					Trans Z :	10.57	11.00	
					Angle X :	-2.82	-2.83	
					Angle Y :	4.28	4.44	
					Angle Z :	-20.30	-20.25	
					Scale X :	0.97	0.96	
					Scale Y :	0.97	0.96	
					Scale Z :	0.97	0.96	

Table 4
Root mean square error (RMSE) of the Registration Algorithm

Dataset	Error								
	Angle x	Angle y	Angle z	Translation x	Translation y	Translation z	Scale x	Scale y	Scale z
Wang et al. (2021)	0.989	0.473	0.432	0.876	0.415	0.670	0.016	0.030	0.046
ST C14	1.411	1.201	1.297	1.501	1.136	1.826	0.102	0.075	0.051
Spurin et al. (2021)	0.345	0.337	0.466	0.429	0.218	0.179	0.039	0.017	0.014

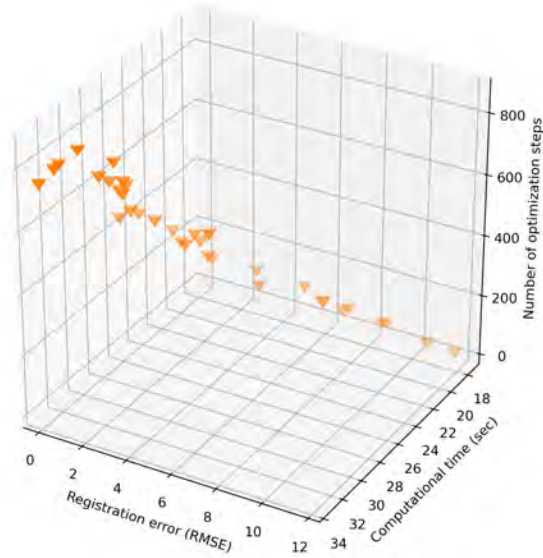


Figure 5: The trade-off between Computational time (sec) vs Registration Error (RMSE) and the Number of Optimization Steps is shown in the figure.

4.7. Timing and Efficiency Analysis

Computational Time We compare the effect of steps in the optimization algorithm in the form of a scatter plot. From the scatter plot in Fig. 5, we can observe that increasing the number of optimization steps generally leads to a better registration error up to a certain point, whereas the computation times needed also increases. This experiment was performed for the dataset provided by Wang et al. (2021) et al.. For each data point in the figure, the average RMSE is calculated for all transformation parameters (translation, rotations and scalings) and multiple runs (50 runs). Using multiple runs ensures that noisy data points are removed.

Human Expert Time Comparison: We compare the speed of our method with those of a human expert in terms of time. The human performance data was only available for ST C14 dataset. Our method takes under 1 minute for most examples. On the other hand, the human expert uses a combination of manual labour and expert tools to achieve the task in 120 minutes. It is also pertinent to note that the human expert performed this transformation for just one case. It was relatively easy, as no inversion of the sample was present in the unregistered image.

5. Conclusion

In this work, we have presented an algorithm for fast and accurate registration of 3D dry and wet digital rock images. We have used a cross-correlation-based optimization process for this task. The process of 3D registration based on optimization is considered slow and usually shunned in many cases due to the advent of one-shot methods. However, one-shot methods either do not provide a robust enough solution or sometimes do not provide a solution at all. Therefore, this work demonstrated that the optimization process could be sped up considerably using GPU. In addition, we provide an algorithm that is robust enough to ensure the high accuracy of the registration solution. We demonstrate the effectiveness of our results under plausible industrial scenarios, such as extreme rotation along the vertical axis and inversion of the sample.

6. Acknowledgment

This work was partially supported by the Norwegian Research Council (grant number 296093) and the members of the SmartRocks joint industry project (ENI AS, Repsol AS, and Chevron Corporation).

References

- Aarnes, J.E., Kippe, V., Lie, K.A., Rustad, A.B., 2007. Modelling of multiscale structures in flow simulations for petroleum reservoirs, in: Geometric Modelling, Numerical Simulation, and Optimization. Springer, pp. 307–360.
- Althof, R.J., Wind, M.G., Dobbins, J.T., 1997. A rapid and automatic image registration algorithm with subpixel accuracy. *IEEE transactions on medical imaging* 16, 308–316.
- Arns, C.H., Knackstedt, M.A., Pinczewski, W.V., Garboczi, E.J., 2002. Computation of linear elastic properties from microtomographic images: Methodology and agreement between theory and experiment. *Geophysics* 67, 1396–1405.
- Avants, B.B., Tustison, N.J., Song, G., Cook, P.A., Klein, A., Gee, J.C., 2011. A reproducible evaluation of ants similarity metric performance in brain image registration. *Neuroimage* 54, 2033–2044.
- Bhattad, P., Young, B., Berg, C.F., Rustad, A.B., Lopez, O., 2014. X-ray micro-ct as-sisted drainage rock typing for characterization of flow behaviour of laminated sandstone reservoirs .
- Chee, E., Wu, Z., 2018. Airnet: Self-supervised affine registration for 3d medical images using neural networks. *arXiv preprint arXiv:1810.02583* .
- Consortium, T.M., 2020. Project monai. URL: <https://doi.org/10.5281/zenodo.4323059>, doi:10.5281/zenodo.4323059.
- De Castro, E., Morandi, C., 1987. Registration of translated and rotated images using finite fourier transforms. *IEEE Transactions on pattern analysis and machine intelligence* , 700–703.
- Feali, M., Pinczewski, W.V., Cinar, Y., Arns, C.H., Arns, J.Y., Turner, M., Senden, T., Francois, N., Knackstedt, M., et al., 2012. Qualitative and quantitative analyses of the three-phase distribution of oil, water, and gas in bentheimer sandstone by use of micro-ct imaging. *SPE Reservoir Evaluation & Engineering* 15, 706–711.
- Fu, Y., Lei, Y., Wang, T., Curran, W.J., Liu, T., Yang, X., 2020. Deep learning in medical image registration: a review. *Physics in Medicine & Biology* 65, 20TR01.
- Haskins, G., Kruecker, J., Kruger, U., Xu, S., Pinto, P.A., Wood, B.J., Yan, P., 2019. Learning deep similarity metric for 3d mr–trus image registration. *International journal of computer assisted radiology and surgery* 14, 417–425.
- Haskins, G., Kruger, U., Yan, P., 2020. Deep learning in medical image registration: a survey. *Machine Vision and Applications* 31, 1–18.
- Hu, Y., Modat, M., Gibson, E., Ghavami, N., Bonmati, E., Moore, C.M., Emberton, M., Noble, J.A., Barratt, D.C., Vercauteren, T., 2018. Label-driven weakly-supervised learning for multimodal deformable image registration, in: 2018 IEEE 15th International Symposium on Biomedical Imaging (ISBI 2018), IEEE. pp. 1070–1074.
- Jenkinson, M., Smith, S., 2001. A global optimisation method for robust affine registration of brain images. *Medical image analysis* 5, 143–156.
- Keszei, A.P., Berkels, B., Deserno, T.M., 2017. Survey of non-rigid registration tools in medicine. *Journal of digital imaging* 30, 102–116.
- Klein, S., Staring, M., Murphy, K., Viergever, M.A., Pluim, J.P., 2009. Elastix: a toolbox for intensity-based medical image registration. *IEEE transactions on medical imaging* 29, 196–205.
- Knackstedt, M., Arns, C., Limaye, A., Sakellariou, A., Senden, T., Sheppard, A., Sok, R., Pinczewski, W.V., Bunn, G., 2004. Digital core laboratory: Properties of reservoir core derived from 3d images, in: SPE Asia Pacific conference on integrated modelling for asset management, OnePetro.
- Krizhevsky, A., Sutskever, I., Hinton, G.E., 2012. Imagenet classification with deep convolutional neural networks, in: Proceedings of the 25th International Conference on Neural Information Processing Systems - Volume 1, Curran Associates Inc., USA. pp. 1097–1105. URL: <http://dl.acm.org/citation.cfm?id=2999134.2999257>.
- Latham, S., Varslot, T., Sheppard, A., et al., 2008. Image registration: enhancing and calibrating x-ray micro-ct imaging. *Proc. of the Soc. Core Analysts, Abu Dhabi, UAE* , 1–12.
- LeCun, Y., Boser, B.E., Denker, J.S., Henderson, D., Howard, R.E., Hubbard, W.E., Jackel, L.D., 1990. Handwritten digit recognition with a back-propagation network, in: Touretzky, D.S. (Ed.), *Advances in Neural Information Processing Systems 2*. Morgan-Kaufmann, pp. 396–404. URL: <http://papers.nips.cc/paper/293-handwritten-digit-recognition-with-a-back-propagation-network.pdf>.
- Liao, R., Miao, S., de Tournemire, P., Grbic, S., Kamen, A., Mansi, T., Comaniciu, D., 2017. An artificial agent for robust image registration, in: Proceedings of the AAAI conference on artificial intelligence.
- Long, H., Nardi, C., Idowu, N., Carnerup, A., Øren, P., Knackstedt, M., Varslot, T., Sok, R., Lithicon, A., 2013. Multi-scale imaging and modeling workflow to capture and characterize microporosity in sandstone 13.
- Maes, F., Collignon, A., Vandermeulen, D., Marchal, G., Suetens, P., 1997. Multimodality image registration by maximization of mutual information. *IEEE transactions on Medical Imaging* 16, 187–198.
- Miao, S., Wang, Z.J., Liao, R., 2016. A cnn regression approach for real-time 2d/3d registration. *IEEE transactions on medical imaging* 35, 1352–1363.
- Padhy, G., Lemaire, C., Amirtharaj, E., Ioannidis, M., 2007. Pore size distribution in multiscale porous media as revealed by ddif–nmr, mercury porosimetry and statistical image analysis. *Colloids and Surfaces A: Physicochemical and Engineering Aspects* 300, 222–234.
- Paszke, A., Gross, S., Chintala, S., Chanan, G., Yang, E., DeVito, Z., Lin, Z., Desmaison, A., Antiga, L., Lerer, A., 2017. Automatic differentiation in pytorch .
- Pratt, W.K., 1974. Correlation techniques of image registration. *IEEE transactions on Aerospace and Electronic Systems* , 353–358.
- Prodanović, M., Lindquist, W., Seright, R., 2007. 3d image-based characterization of fluid displacement in a berea core. *Advances in Water Resources* 30, 214–226.
- Roche, A., Malandain, G., Ayache, N., 2000. Unifying maximum likelihood approaches in medical image registration. *International Journal of Imaging Systems and Technology* 11, 71–80.
- Ruspini, L., Oeren, P.E., Berg, S., Masalmeh, S., Bultreys, T., Taberner, C., Sorop, T., Marcelis, F., Appel, M., Freeman, J., Wilson, O., 2021. Multiscale digital rock analysis for complex rocks. *Transport in Porous Media* 139, 1–25. doi:10.1007/s11242-021-01667-2.
- Sandkühler, R., Jud, C., Andermatt, S., Cattin, P.C., 2018. Airlab: autograd image registration laboratory. *arXiv preprint arXiv:1806.09907* .
- Spurin, C., Krevor, S., Blunt, M., Bultreys, T., 2021. Decane and brine injected into estailades carbonate - steady-state experiments. <http://www.digitalrockportal.org/projects/344>. doi:10.17612/cd7a-y955.
- Viola, P., Wells III, W.M., 1997. Alignment by maximization of mutual information. *International journal of computer vision* 24, 137–154.
- Wang, S., Bultreys, T., Van Offenwert, S., Ruspini, L., 2021. Dataset for unsteady-state capillary drainage experiment on estailades carbonate. <http://www.digitalrockportal.org/projects/363>. doi:10.17612/6rtt-5w16.
- Yoo, T.S., Ackerman, M.J., Lorensen, W.E., Schroeder, W., Chalana, V., Aylward, S., Metaxas, D., Whitaker, R., 2002. Engineering and algorithm design for an image processing api: a technical report on itk-the insight toolkit, in: *Medicine Meets Virtual Reality 02/10*. IOS press, pp. 586–592.